EDGE ARTICLE

Check for updates

Adsorption-mediated efficient glucose electrooxidation on transition metal aerogels for biomass upgradation

Haoxin Fan,[†ab] Xiuming Bu,[†c] Ziqi Wan,[a] Shougang Sun,[d] Hengwei Lou,[a] Xuemei Zhou, [ID][d] Jie Gao, [ID][e] JiaoJiao Miao,[e] Jian Zhang, [ID][a] Wei Gao [ID] *[ab] and Dan Wen [ID] *[a]

The electrocatalytic glucose oxidation reaction (GOR) to produce high value-added chemicals is facilitating the selective conversion and efficient utilization of biomass, while the oxidation products and reaction pathways associated with different transition metals remain insufficiently explored. Herein, the GOR performance on Co, Ni, and Cu metal aerogels was systematically investigated, exhibiting the activity order of Ni > Co > Cu for GOR electrocatalysis. Metal oxyhydroxides (M-OOH) from surface reconstruction of metal aerogels are identified as the actual active species, and the glucose adsorption strength on M-OOH correlated to the GOR properties for metal aerogels are elucidated. *In situ* characterization studies further revealed the interfacial reaction mechanism and reaction pathway on the Ni aerogel with high activity and formic acid selectivity. Besides, the efficient GOR properties of the Ni aerogel further promoted stable water electrolysis at high current densities. Thus, this study offers constructive guidance for designing high-performance GOR electrocatalysts and establishes a feasible prototype for biomass upgradation.

1 Introduction

Exploiting renewable biomass resources as alternatives to conventional fossil resources for fuel and chemical production represents a crucial approach to promote the green and sustainable development.[1–3] Glucose with abundant oxygen-containing functional groups has been investigated as a promising substrate for the production of various carboxylic acid products because of the low cost and high abundance through the electrocatalytic conversion, which attracted increasing concerns in recent years for the upgradation of biomass.[4,5] Fundamentally, the electrocatalytic glucose oxidation reaction (GOR) benefits from superior thermodynamics, manifesting in a lower potential of 0.05 V *versus* the reversible hydrogen electrode (RHE).[6] Thus, the cost-effective and environment friendly

upgradation of glucose through electrocatalysis is also favored to combine with electrocatalytic water reduction in water electrolysis for producing hydrogen and high-value-added products simultaneously.[7,8] Nevertheless, the glucose oxidation pathway featuring alcohol/aldehyde functionalities is intricate with C–C bond cleavage involved,[9,10] which poses significant challenges to comprehend the reacting process and design catalysts for the oriented generation of oxidation products with competitive selectivity.

Lately, transition metal (TM)-based (*e.g.*, Co, Ni, and Cu) catalysts have demonstrated considerable catalytic activity and product selectivity toward the GOR, as explicated by recent research.[11,12] Specifically, engineering nanostructures (*e.g.*, 3D porous networks and nanowire/nanosheet arrays) to amplify specific surface area and active site accelerates GOR kinetics.[13] For instance, Yu *et al.*[14] fabricated the bimetallic NiFeO$_x$ catalysts supported on three-dimensional Ni foam, exhibiting an exceptionally high Faraday efficiency (FE) in the production of glucaric acid from glucose. Besides, Renneckar *et al.*[15] synthesized W-doped nickel–iron phosphide (W-NiFeP) nanosheet arrays *via* ion exchange and phosphidation processes, which significantly improved proton transfer efficiency and the intermediate adsorption, thereby exhibiting outstanding GOR performance. While strategies including alloying,[16,17] elemental doping,[18–20] heterojunction formation,[21] and single-atom design[22] improve TM-based catalysts' intrinsic activity, the role of different metals in governing glucose oxidation pathways and product selectivity

[a] State Key Laboratory of Solidification Processing, School of Materials Science and Engineering, Northwestern Polytechnical University, Xi'an, 710072, P. R. China. E-mail: wei.gao@nwpu.edu.cn; dan.wen@nwpu.edu.cn

[b] Research & Development Institute of Northwestern Polytechnical University in Shenzhen, Shenzhen, 518057, P. R. China

[c] China CAS Key Laboratory of Materials for Energy Conversion, Shanghai Institute of Ceramics, Chinese Academy of Sciences, Shanghai, 200050, P. R. China

[d] Key Laboratory of Carbon Materials of Zhejiang Province, Wenzhou University, Wenzhou, 325035, P. R. China

[e] Interdisciplinary Research Center of Biology & Catalysis, School of Life Sciences, Northwestern Polytechnical University, Xi'an, 710072, P. R. China

† Haoxin Fan and Xiuming Bu contributed equally to this work.

is poorly defined. Therefore, elucidating the glucose oxidation performance and catalytic mechanisms across various metals is imperative to steer the rational design of advanced electrocatalysts toward efficient glucose upgradation.

Based on the above considerations, herein, Co, Ni, and Cu metal aerogels with three-dimensional porous structures were prepared as representative electrocatalysts, and subjected to systematic investigation to elucidate intrinsic activity differences in electrocatalytic glucose conversion. Experimental results demonstrated the order of Ni > Co > Cu for these metal aerogels in electrocatalytic GOR activity and Faraday efficiency for producing formic acid. *In situ* characterization studies and theoretical calculations indicated that the surface metal oxyhydroxide (M-OOH) species derived from corresponding metal aerogels served as the active species for the electrocatalytic GOR, and the activity and selectivity relationships of various metals were established by using the glucose adsorption energy as the descriptor. In addition, when employing the Ni aerogel with the best activity and selectivity for the GOR as the anode catalyst, the glucose oxidation-assisted water electrolysis system can operate stably for more than 30 hours at industrial-grade current density. Therefore, this work elucidated the surface reaction mechanism of the GOR with different transition metal-based catalysts, which may provide a significant guidance for tailored efficient biomass electrocatalysts.

2 Results and discussion

2.1 Structural characterization

Metal aerogels are known for their hierarchical metallic skeleton structures, which facilitate efficient mass transportation and good electrocatalytic properties, enabling their broad applications in electrocatalysis.[23,24] Herein, the three-dimensional Co, Ni, and Cu metal aerogels are employed as the representatives to investigate their performance in the GOR. All metal aerogels were synthesized by an ultrasonic-assisted reduction method (Fig. 1a). Specifically, the metal cations (Co^{2+}, Ni^{2+}, and Cu^{2+}) were rapidly reduced by $NaBH_4$ under ultrasonic cavitation (Fig. S1), subsequently metal aerogels were obtained by supercritical CO_2 drying (Fig. S2). According to weighing and roughly estimating the volume of several samples, the densities of Co, Ni and Cu aerogels are 0.0191, 0.0179 and 0.0249 g cm^{-3}, respectively. Representative scanning electron microscope (SEM) images illustrated the porous morphology and cross-linked nanowire structures for Co, Ni, and Cu aerogels, as depicted in Fig. 1b–d and S3.[25] In Fig. 1e–g, typical transmission electron microscope (TEM) images also exhibited the assembled nanowire morphology, with the average nanoparticle sizes of 15.0 ± 0.3, 27.7 ± 0.3, and 49.9 ± 0.9 nm for Ni, Co, and Cu aerogels, respectively (Fig. 1h). Furthermore, high-resolution TEM (HRTEM) (Fig. 1e–g) displayed the lattice distances of 0.205, 0.203, and 0.209 nm, belonging to the Co (111), Ni (111), and Cu (111) crystal planes, respectively. Besides, X-ray diffraction (XRD) patterns (Fig. 1i) verified the face-centered cubic structures for different aerogels with the main diffraction peak indexing to the (111) crystal plane, which was aligned with the HRTEM observations. Meanwhile, the full

width at half maximum (FWHM) of the peaks for Ni and Co aerogels was significantly broader that that for the Cu aerogel to indicate the smaller particle sizes and lower crystallinity, which matched the TEM characterization well. X-ray photoelectron spectroscopy (XPS) analysis (Fig. S4) revealed the surface chemical states of various aerogels, indicating that the observed metal oxidation states likely result from atmospheric oxidation of the metal surfaces.[26] Compared with the Cu aerogel, the O 1s characteristic peaks of Co and Ni aerogels are relatively stronger, suggesting a higher oxygen content. The oxygen content of the metal aerogels may influence the formation of metal oxyhydroxide to affect the GOR activity. The nitrogen physisorption based on the Brunauer–Emmett–Teller (BET) method was conducted to assess the specific surface area and pore characteristics of the metal aerogels (Fig. 1j). The BET specific surface areas of Co and Ni aerogels were 42.47 and 43.37 $m^2\ g^{-1}$, respectively, whereas the Cu aerogel shows the lower specific surface area of 24.35 $m^2\ g^{-1}$ (Table S1). The corresponding pore size distribution curves obtained from nitrogen desorption data (Fig. S5) further confirm the hierarchical micro/mesoporous structures for Co, Ni, and Cu aerogels.[27] The abundant pore architecture enhances substrate diffusion kinetics by maximizing accessible active sites.

2.2 Evaluation of electrocatalytic GOR performance

To investigate the electrocatalytic performance of different metal aerogels for the oxygen evolution reaction (OER) and GOR, the polarization curves without *iR* compensation (Fig. 2a) were evaluated in 1.0 M KOH with and without 0.1 M glucose solution. Since the GOR has lower thermodynamic potential compared to the OER, the onset potential for the GOR is much smaller than that for the OER after adding glucose into alkaline electrolyte. Observably, Ni and Co aerogels displayed excellent electrocatalytic GOR performance compared to the Cu aerogel. Furthermore, the significant high current density for the GOR compared to the OER affirmed the easier oxidation of glucose (Fig. 2b). In specific, the GOR current density of the Ni aerogel was 260.9 mA cm^{-2} at a potential of 1.60 V (*vs.* RHE), which was much higher than those of Co (147.4 mA cm^{-2}) and Cu (20.1 mA cm^{-2}) aerogels. The intrinsic reaction kinetics were elucidated by the Tafel slope of the GOR (Fig. 2c). The smaller Tafel slope of the Ni aerogel (90.5 mV dec^{-1}) compared with Cu (199.7 mV dec^{-1}) and Co (180.5 mV dec^{-1}) confirmed the faster glucose oxidation kinetics of the Ni aerogel.[28] Furthermore, the charge transfer kinetics of the GOR was evaluated by fitting the electrochemical impedance spectroscopy (EIS) results with an equivalent circuit, as the Nyquist plots given in Fig. 2d and fitting results shown in Table S2. Compared to the Cu aerogel with a charge transfer resistance (R_{ct}) of 35.80 Ω, the lower R_{ct} values of 2.63 and 3.31 Ω for Ni and Co aerogels, respectively, revealed their faster charge transfer properties. The electrochemically active surface area (ECSA) of the catalyst is linearly proportional to the double-layer charging capacitance (C_{dl}), which can be evaluated through cyclic voltammetry measurement. The double layer capacitance values of Co, Ni, and Cu aerogels were 1.19, 1.30, and 1.14 mF cm^{-2}, respectively
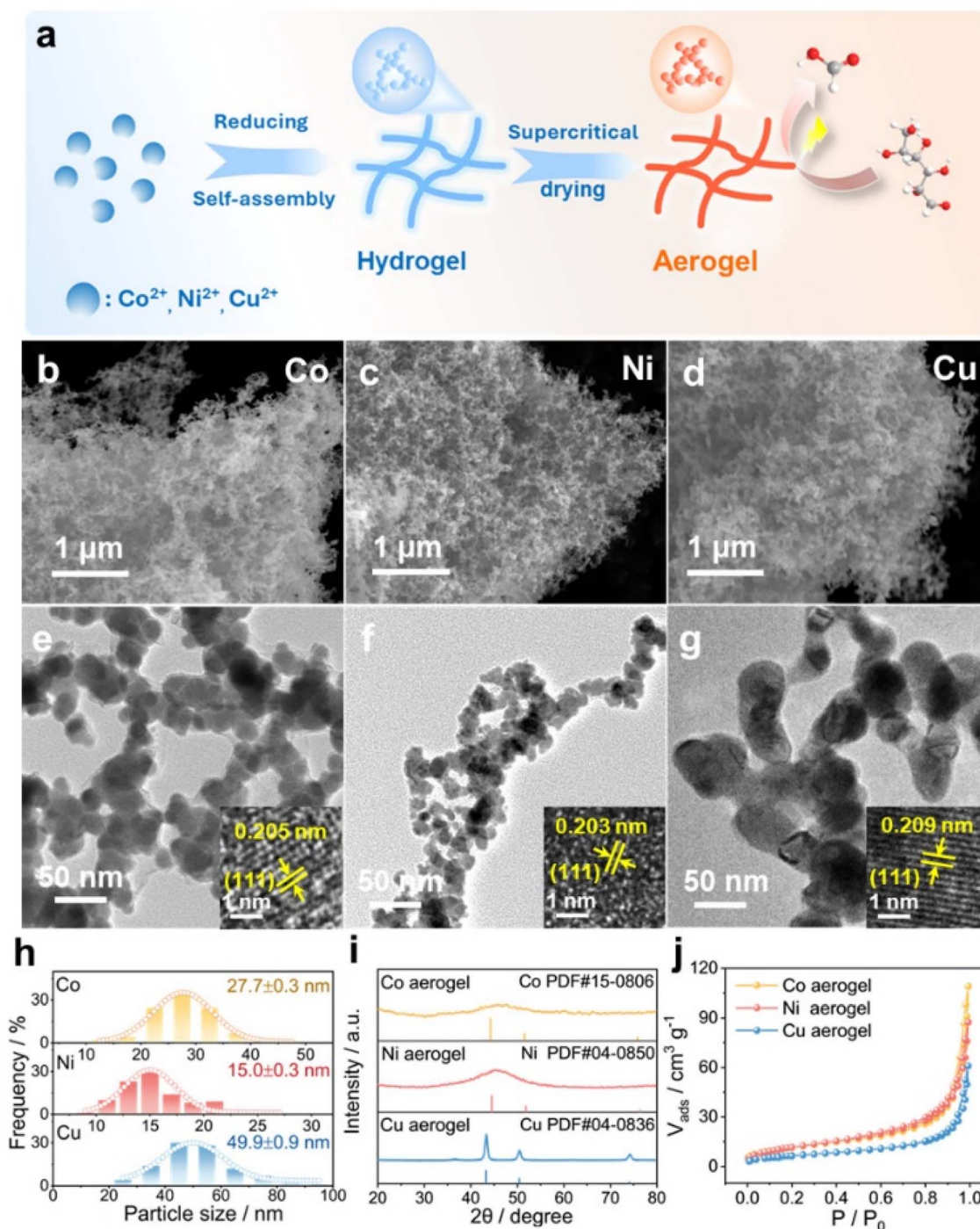
Fig. 1 (a) Schematic illustration of the synthesis of Co, Ni, and Cu aerogels. (b–d) SEM images of (b) Co, (c) Ni, and (d) Cu aerogels, respectively. (e–g) TEM and HRTEM images of (e) Co, (f) Ni, and (g) Cu aerogels, respectively, and (h) the corresponding particle size comparison diagram. (i) XRD patterns and (j) nitrogen physisorption isotherms for various metal aerogels.

(Fig. S6).[29] The polarization curves normalized to ECSA are shown in Fig. 2e, where the higher normalized GOR current density of the Ni aerogel than those of Co and Cu aerogels further suggested the greater GOR intrinsic activity.

In addition, the long-term stability of various aerogels was estimated through the chronopotentiometry method (Fig. S7). Compared to Co and Cu aerogels, Ni aerogels also displayed long-term stability at a current density of 50 mA cm^{-2}. The electrocatalytic glucose oxidation properties of different aerogels were also evaluated at the same potential (Fig. 2f). After injecting 0.1 M glucose solution, the current density of the Ni aerogel at 1.5 V (*vs.* RHE) reached 170.5 mA cm^{-2}, while those of Co and Cu aerogels were 105.8 and 38.7 mA cm^{-2}, respectively. The effect of glucose concentration on the GOR properties was
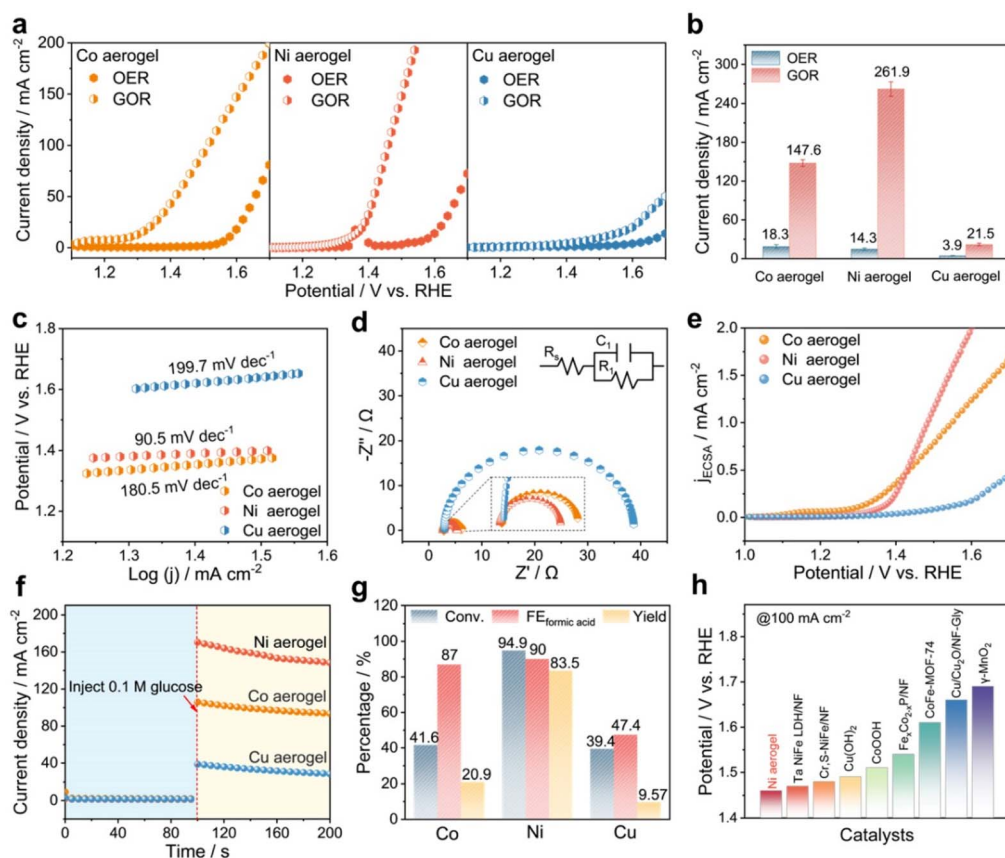
Fig. 2 Electrocatalytic glucose oxidation performance in 1.0 M KOH with 0.1 M glucose for various metal aerogels. (a) Polarization curves of the OER and GOR, (b) the comparison of current density with error bars at a potential of 1.6 V (vs. RHE). (c) Tafel plots, (d) Nyquist plots, (e) GOR activity of different metal aerogels normalized by ECSA, (f) the chronoamperometry at 1.5 V (vs. RHE), (g) glucose conversion, Faraday efficiency and yield of formic acid, (h) the comparison of GOR potential of the Ni aerogel with previously reported catalysts at a current density of 100 mA cm^{-2}.

further investigated utilizing the Ni aerogel (Fig. S8a). The GOR current density of the Ni aerogel increased linearly for the glucose concentrations ranging from 0 to 50 mM, and then tended to a maximum value with increasing glucose concentration (Fig. S8b). To further analyze the GOR products of different aerogels, the *i–t* test was performed in 1.0 M KOH containing 10 mM glucose in combination with high-performance liquid chromatography (HPLC) monitoring (Fig. S9). Among various products, formic acid was the main product of the GOR with higher yield (Fig. S10). As derived from the HPLC results, the Ni aerogel exhibited a glucose conversion of 94.9%, a Faraday efficiency (FE) of 90.0% and a formic acid yield of 83.5%, respectively (Fig. 2g). In contrast, Co and Cu aerogels showed lower glucose conversion (41.6% and 39.4%), FE (87.0% and 47.4%) and formic acid yield (20.9% and 9.57%), respectively. The GOR performance of different aerogels is revealed in Fig. S11 and Table S3. Therefore, the Ni aerogel exhibited the better GOR properties and formic acid selectivity than Co and Cu aerogels, showing the GOR catalytic activity order of Ni > Co > Cu. In addition, the Ni aerogel also exhibits higher GOR performance compared with the previously reported catalysts, indicating its significant potential to produce high value-added products (Fig. 2h and Table S4).

2.3 Identification of the GOR mechanism on various aerogels

To identify the active species on the surface of metal aerogels, the catalysts after the GOR were analyzed by Raman spectroscopy (Fig. S12). According to previous reports, the sharp peaks at 457 and 657 cm^{-1} for the Co aerogel were attributed to the A_{1g} (stretching vibration) and E_g (bending vibration) modes of Co–O, while the vibrational bands around 608 and 508 cm^{-1} were typically associated with amorphous CoOOH.[30,31] Similarly, the Raman peaks at 450 and 523 cm^{-1} for the Ni aerogel could be ascribed to the sharp bands of Ni–O, while the peaks at 476 and 553 cm^{-1} are corresponded to the E_g and A_{1g} vibrational modes of Ni^{3+}–O in NiOOH.[32,33] Furthermore, the Raman peaks at 450 and 550 cm^{-1} for the Cu aerogel can also be assigned to the E_g and A_{1g} vibrational modes of CuOOH.[34] These observations suggested that metal oxyhydroxide (M-OOH) formed on the aerogel surfaces may serve as the active species for the oxidation of glucose (Fig. 3a). To investigate the glucose adsorption ability on different aerogel surfaces, electrochemical glucose stripping measurements were performed (Fig. S13).[35] The oxidation charge of glucose (Glu) was used to quantitatively determine the adsorbed amount of glucose. The results (Fig. 3b) showed that
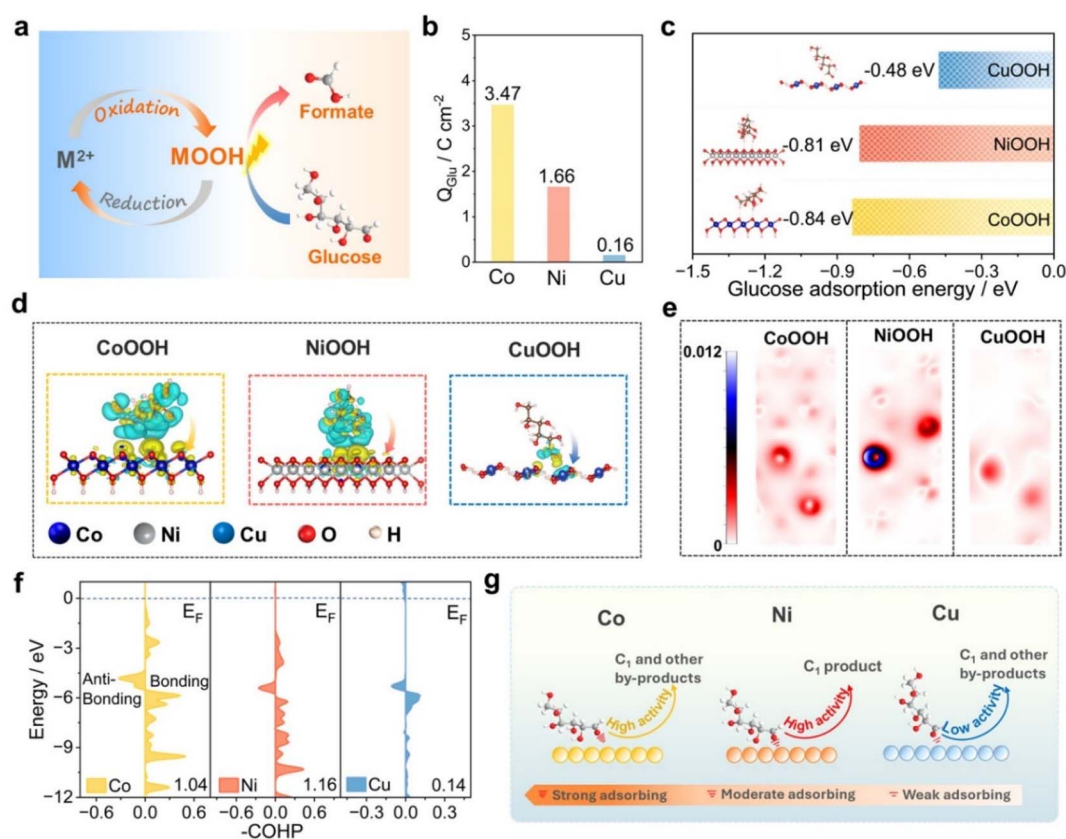
Fig. 3 (a) Proposed mechanism of the electrochemical GOR over the different aerogels. (b) Values of the oxidation charges (QGlu) for adsorbed glucose on different metal aerogels. (c) Adsorption energy of glucose on CoOOH, NiOOH and CuOOH. (d) Bader charge analysis on CoOOH, NiOOH and CuOOH. (e) Corresponding electron localization function evaluations. (f) Crystal orbital Hamilton populations (COHPs) of glucose on CoOOH, NiOOH and CuOOH. (g) GOR diagram within the anode of the inner Helmholtz layer.

the charge (Q) values for Co and Ni aerogels (3.47 and 1.66 C cm^{-2}, respectively) are much higher than that (0.16 C cm^{-2}) for the Cu aerogel, indicating the better glucose adsorption ability for Co and Ni aerogels.

Density functional theory (DFT) calculations were also employed to compare the glucose adsorption abilities of CoOOH, NiOOH, and CuOOH.[36,37] The optimized stable models for glucose adsorption on various MOOH are shown in Fig. S14. The adsorption energies for CoOOH and NiOOH towards glucose were −0.84 and −0.81 eV, respectively, while that for CuOOH was only −0.48 eV (Fig. 3c). This result was consistent with the glucose stripping measurements to illustrate the stronger adsorption of glucose on the surface of Ni and Co aerogels. Furthermore, the differential charge diagram (Fig. 3d) clearly depicted the electronic redistribution at the interface between glucose and metal oxyhydroxides. Evidently, glucose on CoOOH and NiOOH surfaces undergo significant charge transfer from glucose to the MOOH surface, while insignificant charge transfer on CuOOH occurs at the aldehyde group of glucose. Additionally, the local electronic function (Fig. 3e) indicated that the strong interaction between NiOOH and glucose facilitates the efficient cleavage of the C–C bonds in glucose. The bonding between the different metal oxyhydroxides and glucose was further analyzed through crystal orbital

Hamilton population (COHP) plots (Fig. 3f).[38] Theoretical calculations showed that the -ICOHP value for NiOOH-Glu (1.16) was higher than that for CoOOH-Glu (1.04) and CuOOH-Glu (0.14), indicating a stronger bond energy between NiOOH and glucose. A volcano plot was constructed based on the glucose adsorption energy and catalytic activity (Fig. S15). Obviously, the GOR activity of different metals follows the Sabatier principle. Therefore, the metal oxyhydroxides formed on the surfaces of Co, Ni, and Cu serve as the catalytically active species for glucose oxidation (Fig. 3g). The stronger glucose adsorption ability of CoOOH leads to catalyst poisoning during glucose oxidation, resulting in the partial blocking of surface sites with higher activity. Compared with the Ni aerogel, the strong adsorption and weak desorption of intermediates on the surface of the Co aerogel resulted in the rapid decay of oxidation current during the reaction (Fig. S16), leading to the lower selectivity toward formic acid. In contrast, CuOOH with the weak glucose adsorption ability displays poor catalytic activity and product selectivity. Therefore, NiOOH with moderate glucose adsorption ability and excellent catalytic activity is beneficial for the efficient cleavage of the C–C bond in glucose and the generation of formic acid.

Since the Ni aerogel outperforms Co and Cu aerogels in GOR activity due to the moderate adsorption of glucose on its

surface, *operando* EIS was employed to probe the electrochemical evolution of the electrode interface during the GOR (Fig. 4a–c).[39] Typically, the high-frequency region (10^1–10^4 Hz) in the Bode plots is predominantly indexed to the self-oxidation of the catalysts, whereas the low-frequency region (10^{-2}–10^1 Hz) is corresponded to the oxidation resistance at the electrode/electrolyte interface.[40] The surface electro-oxidation of the catalyst in the high-frequency region was visibly apparent at low potentials in Fig. 4a. Elevating the potential to 1.50 V (*vs.* RHE) led to the emergence of a transition peak in the low-frequency region of the Bode plot, and the progressively decreasing phase angle served as an indicator of OER activity. Following the introduction of 0.1 M glucose, no obvious transition peak was observed in the low-frequency region (Fig. 4b) to suggest the preferential occurrence for the GOR.[41] With increasing applied potential, the phase angle peak decreased and shifted to the higher frequencies, demonstrating accelerated interfacial charge transfer through rapid oxidation of glucose molecules. When the potential surpassed 1.50 V (*vs.* RHE), the phase angle peak subtly shifted towards lower frequencies, indicating interfacial competition between OER and GOR processes. Furthermore, the relevant equivalent circuit diagram of the EIS data and corresponding fitting parameters are shown in Tables S5, S6 and Fig. S17.[42] As derived in Fig. 4c, the significant lower value of interfacial resistance for the GOR at low potential compared to that for the OER demonstrated the faster GOR kinetics for the Ni aerogel (Fig. S18). In particular, the R_{ct} value of the GOR at 1.45 V (*vs.* RHE) was 111 times lower than that of the OER for the Ni aerogel, confirming superior charge transfer efficiency and accelerated reaction kinetics in the GOR (Fig. 4c).

Additionally, surface dynamic reconstruction of the Ni aerogel was probed by *in situ* Raman spectroscopy during the OER and GOR processes (Fig. 4d–f).[43] In Fig. 4d, the vibrational band observed at 489 cm^{-1} under the open circuit potential (OCP) was assigned to the Ni^{II}– O bond, whereas the 798 cm^{-1} feature originated from asymmetric stretching vibration of O–Ni–O bridges.[44] In contrast, two emerging peaks at 476 and 553 cm^{-1} were observed during the GOR when the potential reaches 1.35 V (*vs.* RHE) (Fig. 4e), attributed to the bending (δ) and stretching (ν) vibrations of the Ni^{III}–O bond.[45] We speculate that the presence of glucose may accelerate the dehydrogenation process and induce the generation of high-valent metal active sites, thereby enhancing GOR performance. Furthermore, the corresponding isothermal plots (Fig. 4f) provided a clear visualization of the structure evolution process. The potential-dependent behavior of the NiOOH peak showed a distinct maximum in intensity, corresponding to the electrochemical interconversion process between NiOOH and Ni(OH)$_2$. The multi-step potential curve was measured to investigate the glucose oxidation mechanism of the Ni aerogel.[46] The Ni aerogel was initially pre-oxidized at 1.40 V *vs.* RHE in 1.0 M KOH to accumulate high-valent Ni^{3+} species. When the potential reaches OCP, the negative current (yellow line) was observed (Fig. S19) to reveal the reduction of Ni^{3+}–O into Ni^{2+}–OH. This discrepancy with the *in situ* Raman results may be attributed to the CV pre-activation of the Ni aerogel during the electrochemical test, which can be confirmed by the electrochemical test results and Raman spectra (Fig. S20). After injecting 0.1 M glucose into the electrolyte, the reduction current (red line) gradually decreased and then turned to the OCP state. However, when the GOR (blue line) occurs directly, the reduction current
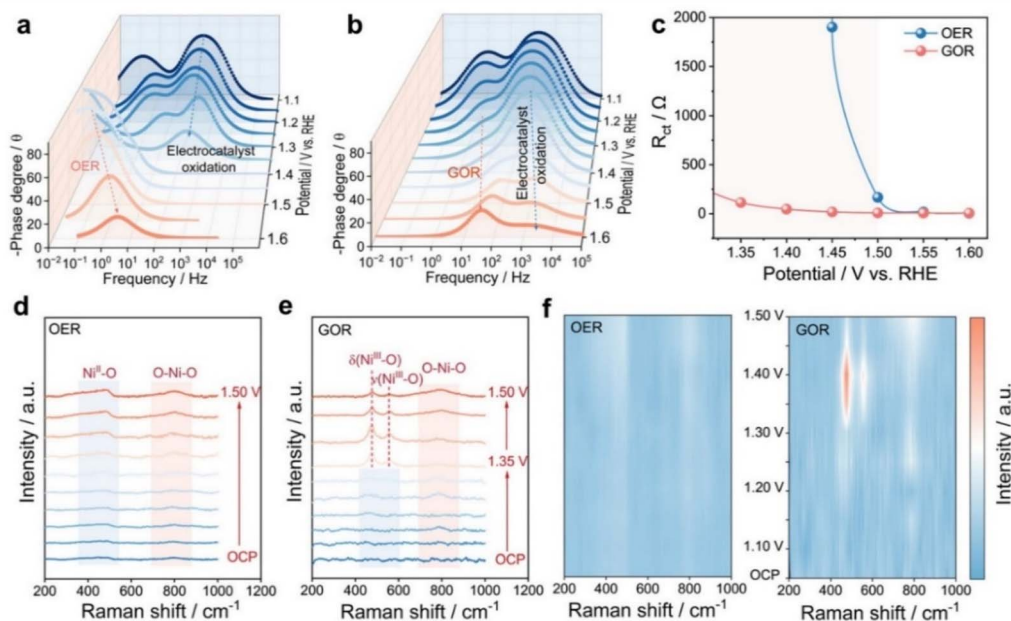

Fig. 4 (a and b) Bode phase plots of *operando* EIS on the Ni aerogel in 1.0 M KOH (a) without and (b) with 0.1 M glucose, and (c) the corresponding resistance of electrode interface reaction (R_{ct}). (d and e) *In situ* Raman spectra (d) without and (e) with 0.1 M glucose in the potential range from OCP to 1.50 V *vs.* RHE, and (f) the corresponding isothermal plots for the OER and GOR.

signal was negligible. Therefore, it is reasonable to speculate the mechanism of the GOR on the Ni aerogel follows the proton coupled electron transfer mechanism. The electrochemical process begins with substrate adsorption at relatively lower potential, followed by potential-dependent activation: (i) $Ni(OH)_2 \rightarrow NiOOH$ transformation, (ii) NiOOH-mediated glucose oxidation to formic acid, and (iii) competitive OER driven by higher potential.

To reveal the reaction pathway of glucose oxidation to formic acid catalyzed by the Ni aerogel, the key intermediates during the GOR were investigated by *operando* attenuated total reflection surface enhanced infrared spectroscopy (ATR-SEIRAS) (Fig. 5a).[47] The appearance of vibrational bands near $1383\ cm^{-1}$ was assigned to carboxyl group formation, demonstrating pronounced potential-induced intensification during electrochemical operation. In addition, gas chromatography (GC) results also verified the replacement of the OER by the GOR and eliminated CO_2 (Fig. S21). The *OH absorption peak near $3300\ cm^{-1}$ was also enhanced with the increase of the potential (Fig. 5b), suggesting that glucose oxidation was closely related to OH^- at the catalytic interface.[48] Furthermore, Fig. S22 displays the alkaline concentration-dependent glucose oxidation performance. The Ni aerogel generated superior current densities in the electrolyte of 1.0 M KOH relative to 0.1 M KOH after introducing 0.1 M glucose. Thus, the principal pathway for glucose oxidation involves the adsorption of both glucose and hydroxyl groups at the electrode interface, followed by sequential dehydrogenation and C–C bond cleavage reactions leading to formic acid.

To quantitatively assess the GOR product, the FE of formic acid by the Ni aerogel at different potentials was evaluated by HLPC (Fig. S23). The FE of formic acid for the Ni aerogel in the potential range of 1.35 to 1.55 V was 99.1%, 98.2%, 94.6%, 86.7%, and 80.1%, respectively. The decrease in FE of formic acid with increasing potentials may be attributed to the competitive OER at higher potentials. Quantitative analysis of formic acid product by the Ni aerogel with different time periods was obtained by collecting solutions at 1.45 V *vs.* RHE (Fig. 5c and Table S7). The signal of glucose decreased gradually and that of formic acid increased significantly with longer reaction times, suggesting the changes in relative concentrations of glucose and formic acid, as shown in Fig. 5d. In addition, five consecutive cycles of *i–t* tests were employed to assess the stability of the Ni aerogel for formic acid production, and the glucose conversion rate was retained at 95.4% after five cycles (Fig. 5e). Besides, the Ni aerogel still retained good catalytic activity and stability after replacing the fresh electrolyte several times during the 100-hour test (Fig. S24). The Ni aerogel after the GOR was collected and characterized *via* TEM (Fig. S25a). Compared to the initial morphology, the three-dimensional structure of the Ni aerogel after the GOR remained intact, and FTIR characterization confirmed the main adsorption of glucose on the surface (Fig. S25b).[49] The post-GOR XRD characterization (Fig. S26) confirmed the partial formation of NiOOH species on the Ni aerogel, corroborating the observations from *in situ* Raman spectroscopy. Simultaneously, XPS analysis (Fig. S27) demonstrated a weaker Ni^0 satellite peak for the Ni aerogel after the *i–t* test and a stronger Ni^{2+} satellite peak that was negatively shifted by 0.5 eV, indicating the surface reconstruction of the Ni aerogel during the GOR. Therefore, above electrochemical analyses explained the good activity, high selectivity toward formic acid, and robust stability of the Ni
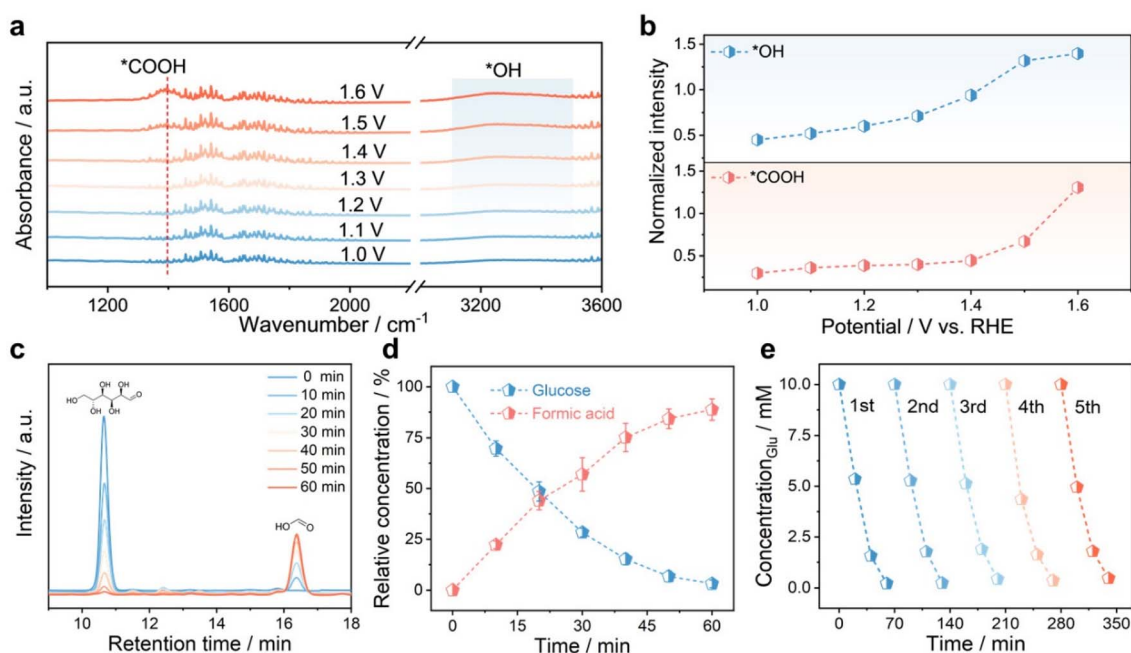

Fig. 5 (a) *In situ* ATR–FTIR spectra of the Ni aerogel collected at potentials ranging from 1.0 to 1.6 V *vs.* RHE with a step of 100 mV, and (b) corresponding intensities of *OH and *COOH signals at different GOR potentials. (c) HPLC chromatograms of the electrolyte at 1.45 V (*vs.* RHE), (d) corresponding ratios of glucose and formic acid signal at different times, and (e) cycling stability.
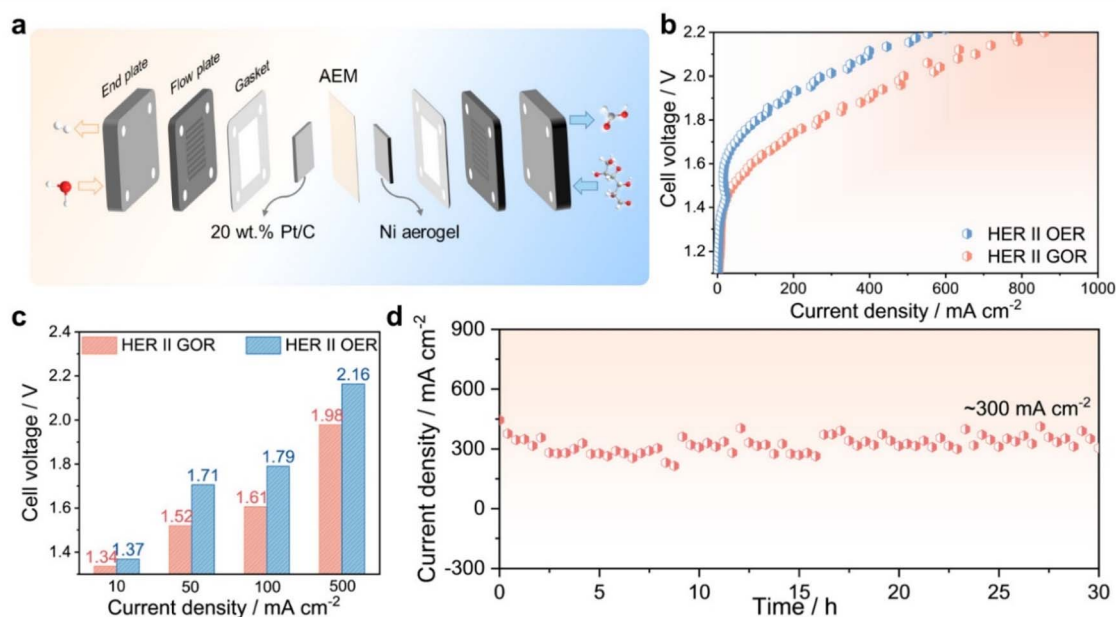
Fig. 6 (a) Schematic diagram of the glucose oxidation coupled water electrolysis system. (b) Polarization curves of the GOR-assisted AEMWE, (c) corresponding cell voltages at various current densities with (red bars) and without (blue bars) 0.1 M glucose, and (d) chronopotentiometry test in which the electrolyte was changed every hour.

aerogel as the anodic electrocatalyst for the electrocatalytic conversion of glucose into formic acid.

2.4 Upgradation of glucose in the water electrolysis system

Given the outstanding GOR performance of the Ni aerogel, we developed an efficient electrochemical system for glucose upgradation. The anion exchange membrane water electrolyzer (AEMWE) was assembled by employing the Ni aerogel as the anode and commercial Pt/C as the cathode, respectively, to realize the GOR-assisted water splitting at room temperature (Fig. 6a).[50] When replacing the OER with the GOR as the anodic reaction, the cell voltage required to achieve the ideal current density was significantly reduced (Fig. 6b). Remarkably, the AEMWE device with 0.1 M glucose in 1.0 M KOH solution only demands voltages of 1.34, 1.52, 1.61, and 1.98 V, to supply current densities of 10, 50, 100, and 500 mA cm^{-2}, respectively, which are lower than those of 1.37, 1.71, 1.79, and 2.16 V for the overall water splitting (Fig. 6c). In addition, by replacing the fresh electrolyte every hour, the activity of the GOR-assisted electrolysis system still remained about 91.8% after 30 cycles of operation at a current density of about 300 mA cm^{-2} (Fig. 6d). The used Ni aerogel was characterized by TEM, as presented in Fig. S28. It was observed that the Ni aerogel underwent surface reconstruction, forming a large amount of hydroxide layer and NiOOH active species. The cathode and anode products collected in a short time were determined by GC and HPLC (Fig. S29), and the FE of hydrogen and formic acid was 99.8% and 90.8%, respectively. Notably, the Ni aerogel also demonstrated remarkable universality, enabling electrocatalytic oxidation of other small organic molecules such as methanol, ethylene glycol, glycerol, fructose, sucrose, and maltose (Fig. S30). In general, we disclosed the GOR mechanism

through various metal aerogels, verified the Ni aerogel as the efficient and stable electrocatalyst for biomass oxidation, enabled simultaneous energy-efficient hydrogen evolution and high value-added chemical production.

3 Conclusions

In this study, we uncovered the difference in electrocatalytic oxidation of glucose for various metal (Co, Ni, and Cu) aerogels and comprehended the catalytic mechanism through experimental and theoretical analyses. Electrochemical tests showed that the glucose oxidation performance and faradaic efficiency for formic acid production follow the trend Ni > Co > Cu. Theoretical calculations confirmed that the glucose adsorption strength as the reactivity descriptor on the metal oxyhydroxide catalytic sites for metal aerogels follows the Sabatier principle, while the Ni aerogel with surface NiOOH species demonstrated moderate glucose adsorption energy, resulting in excellent glucose catalytic activity and formic acid selectivity. Furthermore, *in situ* characterization reveals the dynamic active sites and the proton-coupled electron transfer mechanism during the GOR catalyzed by the Ni aerogel. Building on these findings, we efficiently realized the upgradation of glucose into formic acid by constructing a glucose oxidation-coupled water electrolysis system utilizing Ni aerogel anodes, achieving continuous production of hydrogen and formic acid at near-industrial current densities. Overall, this work elucidates comprehensive insights into the GOR catalytic mechanism and demonstrates a rational framework for developing transition metal-based catalysts for biomass conversion, offering significant potential for high-value biomass applications.

Author contributions

HaoXin Fan: writing – original draft, investigation, methodology, data curation, validation. Xiuming Bu: investigation, data curation, formal analysis. Ziqi Wan: conceptualization, data curation, visualization. Shougang Sun: data curation, visualization. Hengwei Lou: data curation, formal analysis. Xuemei Zhou: data curation, visualization. Jie Gao: conceptualization, formal analysis. Jiaojiao Miao: investigation, formal analysis. Jian Zhang: methodology, visualization. Wei Gao: conceptualization, data curation, investigation, writing – review & editing. Dan Wen: supervision, funding acquisition, writing – review & editing.

Conflicts of interest

The authors declare that they have no known competing financial interests or personal relationships that could have appeared to influence the work reported in this paper.

Data availability

Data will be made available on request.

The data supporting this article have been included as part of the supplementary information (SI). Supplementary information: includes experimental section, additional characterizations, electrochemical data, and supplementary tables. See DOI: https://doi.org/10.1039/d5sc05524e.

Acknowledgements

References

1 M. P. J. M. Van der Ham, J. Creus, J. H. Bitter, M. T. M. Koper and P. P. Pescarmona, *Chem. Rev.*, 2024, **124**, 11915–11967.

2 Y. Lu, M. Chen, Y. Wang, C. Yang, Y. Zou and S. Wang, *Chem*, 2024, **10**, 1371–1390.

3 R. Bai, Z. Zhao, M. Liu, W. Ma, J. Lin, S. An, J. He, Z. Liu, L. Zhang, H. Mei and J. Zhang, *J. Am. Chem. Soc.*, 2025, **147**, 6880–6885.

4 Q. Shi, W. Tang, K. Kong, X. Liu, Y. Wang and H. Duan, *Angew. Chem., Int. Ed.*, 2024, **63**, e202407580.

5 J. Lin, Z. Liu, H. Wu, Z. Wang, G. Wang, J. Bu, Y. Wang, P. Liu, J. Wang and J. Zhang, *Nat. Catal.*, 2025, **8**, 338–347.

6 J. Yang, T. Xia, H. Li, H. Yan, X. Kong, Z. Li, M. Shao and X. Duan, *Angew. Chem., Int. Ed.*, 2024, **64**, e202413457.

7 X. Liu, J. Tang, Y. Chen, X. Song, J. Guo, G. Wang, S. Han, X. Chen, C. Zhang, S. Dou, H. Shao and D. Wang, *ACS Catal.*, 2025, **15**, 7308–7339.

8 D. Li, Z. Li, R. Zou, G. Shi, Y. Huang, W. Yang, W. Yang, C. Liu and X. Peng, *Appl. Catal., B*, 2022, **307**, 121170.

9 H. Zhou, Y. Ren, B. Yao, Z. Li, M. Xu, L. Ma, X. Kong, L. Zheng, M. Shao and H. Duan, *Nat. Commun.*, 2023, **14**, 5621.

10 N. Xi, Y. Zang, X. Sun, J. Yu, M. Johnsson, Y. Dai, Y. Sang, H. Liu and X. Yu, *Adv. Energy Mater.*, 2023, **13**, 2301572.

11 H. Lou, Y. Yang, X. Bu, H. Fan, D. Weng, J. Zhang, W. Gao and D. Wen, *J. Mater. Chem. A*, 2025, **13**, 1067–1073.

12 Z. Yang, B. Zhang, C. Yan, Z. Xue and T. Mu, *Appl. Catal., B*, 2023, **330**, 122590.

13 H. Sun, L. Li, Y. Chen, H. Kim, X. Xu, D. Guan, Z. Hu, L. Zhang, Z. Shao and W. Jung, *Appl. Catal., B*, 2023, **325**, 122388.

14 W. J. Liu, Z. Xu, D. Zhao, X. Q. Pan, H. C. Li, X. Hu, Z. Fan, W. K. Wang, G. H. Zhao, S. Jin, G. W. Huber and H. Yu, *Nat. Commun.*, 2020, **11**, 265.

15 N. Wei, S. Zhang, X. Yao, Q. Li, N. Li, J. Li, D. Pan, Q. Liu, S. Chen and S. Renneckar, *Adv. Sci.*, 2025, **12**, 2412872.

16 S. Liu, S. Dou, J. Meng, Y. Liu, Y. Liu and H. Yu, *Appl. Catal., B*, 2023, **331**, 122709.

17 L. He, M. Li, L. Qiu, S. Geng, Y. Liu, F. Tian, M. Luo, H. Liu, Y. Yu and S. Guo, *Nat. Commun.*, 2024, **15**, 2290.

18 H. Qin, Y. Ye, G. Lin, J. Zhang, W. Jia, W. Xia and L. Jiao, *ACS Catal.*, 2024, **14**, 16234–16244.

19 M. Deng, W. Yang, K. Xiong, H. Zhang, J. Chen, M. Yang and X. Gan, *Int. J. Hydrogen Energy*, 2025, **137**, 1300–1307.

20 S. Wang, Y. Yan, Y. Du, Y. Zhao, T. Li, D. Wang, P. Schaaf and X. Wang, *Adv. Funct. Mater.*, 2024, **34**, 2404290.

21 J. Wu, Z. Zhai, T. Yu, X. Wu, S. Huang, W. Cao, Y. Jiang, J. Pei and S. Yin, *J. Energy Chem.*, 2023, **86**, 480–489.

22 Q. Fang, J. Wen, H. Wang, X. Wei, L. Jiao, X. Luo, M. Sha, Y. Qin, M. Liu, L. Zheng, W. Gu, H. Zhong, L. Hu and C. Zhu, *Nano Energy*, 2024, **13**, 1110217.

23 H. Liu, Y. Tang, T. Jiang, R. Luo, J. Chen, Z. Zhang, J. Xu, D. Shen, Z. Pan, S. Wei, S. Tan, Y. Wang, G. Zhao, Y. Feng, X. Li and W. Chen, *Adv. Funct. Mater.*, 2025, 2419078.

24 Z. Li, B. Li and C. Yu, *Adv. Mater.*, 2023, **35**, 2211221.

25 Y. Chen, X. Wan, G. Li, J. Ye, J. Gao and D. Wen, *Adv. Funct. Mater.*, 2024, **34**, 2404329.

26 H. Fan, X. Wan, S. Sun, X. Zhou, X. Bu, J. Ye, R. Bai, H. Lou, Y. Chen, J. Gao, J. Zhang, W. Gao and D. Wen, *Adv. Energy Mater.*, 2025, 2405681.

27 Q. Fang, S. Ye, L. Zheng, H. Wang, L. Hu, W. Gu, L. Wang, L. Shi and C. Zhu, *ACS Catal.*, 2024, **14**, 9235–9243.

28 Y. Yang, D. Xu, B. Zhang, Z. Xue and T. Mu, *Chem. Eng. J.*, 2022, **433**, 133842.

29 C. Liang, P. Zou, A. Nairan, Y. Zhang, J. Liu, K. Liu, S. Hu, F. Kang, H. J. Fan and C. Yang, *Energy Environ. Sci.*, 2020, **13**, 86–95.

30 T. Vo, P. Ho and C. Chiang, *Appl. Catal., B*, 2022, **300**, 120723.

31 A. Moysiadou, S. Lee, C. Hsu, H. Chen and X. Hu, *J. Am. Chem. Soc.*, 2020, **142**, 11901–11914.

32 P. Xu, Z. Bao, Y. Zhao, L. Zheng, Z. Lv, X. Shi, H. Wang, X. Fang and H. Zheng, *Adv. Energy Mater.*, 2023, **14**, 2303557.

33 S. Lee, Y. C. Chu, L. Bai, H. Chen and X. Hu, *Chem Catal.*, 2023, **3**, 100475.

34 Y. Deng, A. Handoko, Y. Du, S. Xi and B. Yeo, *ACS Catal.*, 2016, **6**, 2473–2481.

35 C. Liu, G. Zhang, W. Zhang, Z. Gu and G. Zhu, *Proc. Natl. Acad. Sci. U. S. A.*, 2023, **120**, e2209979120.

36 Y. Yan, J. Zhong, R. Wang, S. Yan and Z. Zou, *J. Am. Chem. Soc.*, 2024, **146**, 4814–4821.

37 Z. Fan, Q. Yang, W. Zhang, H. Wen, H. Yuan, J. He, H. Yang and Z. Chen, *Nano Lett.*, 2023, **23**, 11314–11322.

38 Y. Xin, L. Chen, Y. Li and K. Shen, *Nano Res.*, 2024, **17**, 2509–2519.

39 W. Xia, K. Yuan, X. Cao, H. Qin, G. Lin, J. Zhang, T. Jin, Q. Wang and L. Jiao, *ACS Catal.*, 2025, **15**, 768–779.

40 Y. Wang, Y. Zhu, Z. Xie, S. Xu, M. Xu, Z. Li, L. Ma, R. Ge, H. Zhou, Z. Li, X. Kong, L. Zheng, J. Zhou and H. Duan, *ACS Catal.*, 2022, **12**, 12432–12443.

41 L. Wu, Q. Wu, Y. Han, D. Zhang, R. Zhang, N. Song, X. Wu, J. Zeng, P. Yuan, J. Chen, A. Du, K. K. Huang and X. Yao, *Adv. Mater.*, 2024, **36**, 2401857.

42 W. Luo, H. Tian, Q. Li, G. Meng, Z. Chang, C. Chen, R. Shen, X. Yu, L. Zhu, F. Kong, X. Cui and J. Shi, *Adv. Funct. Mater.*, 2023, **34**, 2306995.

43 Q. Xue, Z. Xia, W. Gou, J. Bu, J. Li, H. Xiao and Y. Qu, *ACS Catal.*, 2023, **13**, 400–406.

44 J. Wang, W. Zhao, H. Yu, W. Wang, Y. Xu, L. Shen, G. Zhang and D. Mei, *Appl. Catal., B*, 2024, **353**, 124086.

45 X. Zhang, S. Yu, J. Chen, K. Gao, H. Yu and Y. Yu, *Adv. Mater.*, 2025, **37**, 2419050.

46 W. Chen, C. Xie, Y. Wang, Y. Zou, C. L. Dong, Y. C. Huang, Z. Xiao, Z. Wei, S. Du, C. Chen, B. Zhou, J. Ma and S. Wang, *Chem*, 2020, **6**, 2974–2993.

47 W. Chen, L. Zhang, L. Xu, Y. He, H. Pang, S. Wang and Y. Zou, *Nat. Commun.*, 2024, **15**, 2420.

48 J. Zhu, L. Xia, R. Yu, R. Lu, J. Li, R. He, Y. Wu, W. Zhang, X. Hong, W. Chen, Y. Zhao, L. Zhou, L. Mai and Z. Wang, *J. Am. Chem. Soc.*, 2022, **144**, 15529–15538.

49 T. Faverge, B. Gilles, A. Bonnefont, F. Maillard, C. Coutanceau and M. Chatenet, *ACS Catal.*, 2023, **13**, 2657–2669.

50 P. Wang, J. Zheng, X. Xu, Y. Zhang, Q. Shi, Y. Wan, S. Ramakrishna, J. Zhang, L. Zhu, T. Yokoshima, Y. Yamauchi and Y. Long, *Adv. Mater.*, 2024, **36**, 2404806.